Available online at www.sciencedirect.com

ScienceDirect

Acta Materialia 72 (2014) 80–98

Acta MATERIALIA

www.elsevier.com/locate/actamat

Nucleation kinetics of entrained eutectic Si in Al–5Si alloys

J.H. Li [a,*], M.Z. Zarif [a], M. Albu [b], B.J. McKay [a,1], F. Hofer [b], P. Schumacher [a,c]

[a] Institute of Casting Research, University of Leoben, Leoben, Austria
[b] Institute for Electron Microscopy and Fine Structure Research (FELMI), Graz University of Technology, Center for Electron Microscopy, Graz, Austria
[c] Austrian Foundry Research Institute, Leoben, Austria

Received 1 February 2014; received in revised form 11 March 2014; accepted 14 March 2014

Abstract

A series of high-purity Al–5 wt.% Si alloys with trace additions of Sr, Fe and P were prepared by using arc-melting and subsequent melt-spinning. The nucleation phenomenon incorporating the free growth criterion of eutectic Si was investigated by using the entrained droplet technique, atomic resolution scanning transmission electron microscopy and differential scanning calorimetry. It was found that Sr addition exerts no positive effect on the nucleation process; instead, an increased undercooling was observed. A combined addition of Sr and Fe further increased the undercooling, as compared with the addition of Sr only. Only trace P addition has a profound effect on the nucleation of Si by a proposed formation of AlP patches on primary Al. The estimated AlP patch size was found to be sufficient for the free growth of Si to occur inside the eutectic droplet. Nucleation kinetics was discussed on the basis of classical nucleation theory and the free growth model. For the first time, realistic and physically meaningful nucleation site values were obtained. The interactions between Sr and P were also highlighted. This investigation demonstrates strong experimental supports for the free growth nucleation kinetics and the well-accepted impurity-induced twinning growth mechanism, as well as the poisoning of the twin plane re-entrant edge growth mechanism.

Keywords: Al–Si alloys; Nucleation kinetics; Eutectic solidification; Free growth; Melt-spinning

1. Introduction

Al–Si-based alloys are important casting alloys, and constitute ~90% of all shape castings [1]. Primary Si, eutectic Si and other intermetallics, i.e. β-Al_5FeSi, are present in Al–Si-based alloys. The size and shape of eutectic Si in hypoeutectic Al–Si alloys play a major role in determining the final mechanical properties of the manufactured parts, in particular fracture elongation. The eutectic Si of these Al–Si alloys is usually modified by chemical additions of Sr or Na. The phenomenon of modification was first discovered by Pacz [2]. Since then, this scientific discovery is the subject of publications [3–23] to elucidate the physical metallurgical phenomena involved. Nevertheless, the nucleation and growth mechanisms during modification are still a matter of debate. Generally, higher undercoolings are observed for both nucleation and growth during thermal analysis, suggesting that nucleation is depressed and subsequent growth is also hindered [12].

Regarding the aspect of growth, early research [6] proposed that Na addition caused the obstruction of Si crystal growth by surface adsorption of Na on Si. Interestingly, it was postulated as early as 1950 that Si crystal growth may be obstructed via the presence of Na-rich [$NaAlSi_{1.25}$] or [$NaAlSi_{1.33}$] compounds [7]. Plumb and Lewis [8] suggested that the Na addition retarded the nucleation of Si through

* Corresponding author. Tel.: +43 3842 402 3304; fax: +43 3842 402 3302.
E-mail address: jie-hua.li@hotmail.com (J.H. Li).
[1] Present address: BCAST, Brunel University, Uxbridge, Middlesex, UK.

http://dx.doi.org/10.1016/j.actamat.2014.03.030
1359-6454/

its adsorption on the nuclei interface, during eutectic solidification. Wagner [9] and Hamilton and Seidensticker [10] proposed a twin plane re-entrant edge (TPRE) growth mechanism in Ge dendrites. They proposed that growth occurred more readily at the re-entrant edges, which could play a key role in the modification of Ge crystals. Based on the observations of Wagner [9] and Hamilton and Seidensticker [10], as well as the concept of surface adsorption, Day and Hellawell proposed the poisoning of TPREs [3] in 1968. It was assumed that the modifier retarded Si growth by selectively adsorbing at the TPRE, and thus deactivating the growth advantage of the TPRE mechanism. Furthermore, in 1987, Hellawell [11] and Lu and Hellawell [12] developed a growth mechanism after conducting experiments with the additions of impurities, i.e. Na and Sr, and postulated that these impurities were adsorbed on the growing surfaces of Si and caused frequent twinning to occur, which they named as impurity-induced twinning (IIT). It should be noted that either the poisoning of the TPRE mechanism [3] or the IIT mechanism [12] can be attributed to the interfacial poisoning of Si at the growing interface, highlighting the importance of the adsorption of modifier atoms on the growing interface. The main difference is the interfacial poisoning position. For poisoning of the TPRE, interfacial poisoning was proposed to occur at the re-entrant edges, while for IIT, interfacial poisoning was proposed to take place at the ledges (i.e. step or kink sites) on the already growing atomic layers. Both IIT and poisoning of TPRE mechanisms have been experimentally investigated in the case of Sr [5,13–16], although micro X-ray fluorescence spectroscopy mapping [13,14] reveals that Sr is homogenously distributed within the eutectic Si, while energy-dispersive X-ray spectroscopy (EDX) mapping using scanning transmission electron microscope (STEM) and atom probe tomography (APT) [15] show that two types of Al–Si–Sr clusters are distributed at the re-entrant edges and Si growing plane, respectively. This difference may be due to the techniques and resolution used; however, the adsorption of Sr within eutectic Si indeed causes a fine fibrous morphology. A similar experimental observation using the electron probe microanalysis technique (EPMA) also shows that Sr resides mostly inside the Si in an A356 alloy [16]. However, it should be noted that most of these investigations are based on commercial purity Al–Si based alloys produced using conventional casting. It has been reported that there is an important impurity effect on the nucleation and growth of eutectic Si in Al–Si-based alloys [17]. The research on high purity Al–Si alloys is of great interest to elucidate the impurity effect on the nucleation and growth of Si, as suggested by Cho et al. [18]. It is of great necessity to reveal the atomic distribution of Sr within Si particles in extreme cases of high cooling, such as melt-spinning, and under controlled slow cooling in entrained droplets. However, the low Sr concentrations used and the interplay between Si twins and Sr solutes at the re-entrant edge make this observation very challenging.

With respect to nucleation, much more detailed research is required to elucidate the nucleation kinetics during modification. Crosley and Mondolfo [19] reported the poisoning effect of Na on P containing hypoeutectic Al–Si alloys. Na addition forces the nucleation of Si to larger undercoolings. This was attributed to the formation of Na_3P compounds which reduced the amount of the potent AlP phase. Furthermore, Crosley and Mondolfo [19] emphasized that nucleation has a major influence on the modification and AlP could be the nucleation site for eutectic Si due to its excellent match with Si [20–22]. Nogita et al. [20] found the evidence of centrally located AlP particles surrounded by a Si crystal in a hypoeutectic Al–Si alloy containing 40 ppm P. Similar results were also obtained by Ho and Cantor [17] in entrained droplet experiments. Flood and Hunt [23], using quench experiments, demonstrated that Na addition not only changed the growth morphology, but also prevented the nucleation ahead of the eutectic growth front. This produced higher undercoolings and therefore a finer eutectic lamellar spacing. Cho et al. [18] discussed the poisoning effect of Sr on the AlP compound. They proposed that the intermetallic compound Al_2Si_2Sr consumed the AlP, thus reducing the number of nucleated eutectic grains. Clearly, there is an important interaction between the modified elements (i.e. Na, Sr) and P.

If Na or Sr addition poisons the AlP, as proposed in the literature [18–23], an obvious question arises to the nature of the remaining nucleation sites to nucleate Si. Al_2O_3 and SiO_2 impurity particles [24], oxide bi-films [25] and the Al_4Sr phase [26] have been suggested to promote the nucleation of eutectic Si. In addition, the role of Fe-containing intermetallics as a nucleating agent for eutectic Si is also a particular matter of debate. Ho and Cantor [17,27] reported on Al–Si alloys prepared using high-purity materials containing only 50 ppm Fe and considered this amount of Fe as an insignificant impurity. However, Shankar et al. [28,29] proposed that small quantities of Fe (as small as 12 ppm) play an important role in the nucleation of eutectic Si. Khalifa et al. [30] and Yang et al. [31] also suggested that β-Al_5FeSi could be a nucleation site for eutectic Si in hypoeutectic Al–Si alloys. The main reason for the high number of potential types of the nucleation sites may be due to the fact that nucleation is notoriously difficult to study because of the inherent presence of impurities. It was Wang and Smith [32] who first suggested a novel entrained droplet technique to study heterogeneous nucleation. The potential of this technique was recognized and developed further by Cantor and co-workers [17,27,33,34], who employed rapid solidification to produce micrometer- to nanometer-size droplets, thereby improving the reproducibility of nucleation undercooling by up to 0.2 °C. Ho and Cantor [17] studied high-purity Al–Si alloys containing traces of P using the entrained droplet technique [32] and found that just 0.25–2 ppm P is sufficient to form AlP which could act as a nucleation site for eutectic Si, verifying the results of Crosley and Mondolfo [19] and

Flood and Hunt [23]. However, the interaction between Sr and P has not been reported yet.

In this paper, the entrained droplet technique was employed to investigate the influence of trace elements of Sr, Fe and P on the nucleation and growth of entrained eutectic Si in high purity Al–5 wt.% Si alloys, with a special focus on (i) the influence of Sr on Si twinning; and (ii) the interactions between Sr and P. A comparative study is provided to elucidate which compound is more potent to nucleate eutectic Si. The nucleation kinetics are discussed on the basis of the classical nucleation theory [18] and the free growth model [35,36], respectively.

2. Experimental material and procedures

Al–5 wt.% Si alloys (wt.% is used through this paper unless specified otherwise) with controlled additions of Sr, Fe and P were manufactured. For the experimental details about sample preparation, arc-melting, melt-spinning and differential scanning calorimetry (DSC) analysis, see Ref. [37]. The measured composition and undercooling (ΔT) from the DSC analysis are listed in Table 1. Quantitative composition data were obtained using optical emission spark analysis. Other impurity contents, i.e. Ba, Cu, Mn, Mg, etc., were found to be <4 ppm. P content was measured using glow discharge mass spectroscopy (GDMS).

The DSC results were reproducible within 0.2 °C for three subsequent runs on one sample. In order to elucidate the nucleation kinetics of entrained eutectic Si, a series of DSC experiments with different cooling rates (4, 5, 6, 8, 10, 12 and 15 °C min^{-1}) were performed for four different alloys (high purity (5 N Al and 5 N Si) Al–5Si alloy, medium purity (5 N Al and 4 N Si) Al–5Si alloy, high purity Al–5Si–20 ppm Sr alloy and Al–5Si–20 ppm Sr–55 ppm Fe alloy).

Table 1
The compositions obtained by OES spark analysis and undercooling (ΔT) measured from the DSC analysis of high purity Al–5Si alloys with the Sr, Fe and/or P additions (DSC heating and cooling rate: 10 °C min^{-1}).

No.	Alloy compositions	Undercooling ΔT (°C)
1	Al–5 wt.% Si (5 N Al + 4 N Si)	~20.5
2	Al–5 wt.% Si (5 N Al + 5 N Si, 0.4 ppm P)	~31.0
3	Al–5 wt.% Si–0.5 ppm P	~16.1
4	Al–5 wt.% Si–3 ppm P	~2.0
5	Al–5 wt.% Si–5 ppm P	~0.0
6	Al–5 wt.% Si–20 ppm Sr	~49.5
7	Al–5 wt.% Si–50 ppm Sr	~49.5
8	Al–5 wt.% Si–100 ppm Sr	~49.5
9	Al–5 wt.% Si–200 ppm Sr	~49.5
10	Al–5 wt.% Si–25 ppm Fe	~31.0
11	Al–5 wt.% Si–55 ppm Fe	~26.0
12	Al–5 wt.% Si–75 ppm Fe	~26.0
13	Al–5 wt.% Si–200 ppm Fe	~14.0
14	Al–5 wt.% Si–2000 ppm Fe	~14.0
15	Al–5 wt.% Si–55 ppm Fe–20 ppm Sr	~54.5
16	Al–5 wt.% Si–55 ppm Fe–100 ppm Sr	~54.5
17	Al–5 wt.% Si–1 ppm P–50 ppm Sr	~38.0

Note: P* content was measured using GDMS.

The ribbons for scanning electron microscopy (SEM) investigation were mechanically ground and electropolished in a solution consisting of 5% perchloric acid and 95% methanol at –30 °C. The ribbons for transmission electron microscopy (TEM) investigation were mechanically ground, polished and dimpled to ~30 μm, and then ion-beam-milled using a Gatan Precision Ion Polishing System (PIPS, Gatan model 691). A preparation temperature (~–10 °C) was kept constant by using a cold stage during ion beam polishing. Conventional TEM was performed using a Philips CM12 microscope operated at 120 kV equipped with a CCD-camera (GATAN Model 794 MSC BioScan). The high-resolution STEM micrographs and EDX were performed using an FEI Titan^{3}™ G2 60–300 (S/TEM) monochromated and probe corrected microscope operated at 300 kV with a beam diameter of 0.1 nm and 0.039 nA current. Elemental quantification of the EDX spectra was performed by using the zeta factor method [38].

3. Results

3.1. Alloys with varying degree of P

3.1.1. As-spun ribbon microstructure

Fig. 1a shows a typical microstructure in high purity melt-spun Al–5Si–5 ppm P alloy. Some Si particles are distributed either along the grain boundary, or within the α-Al matrix. One Si particle was tilted to the principal twinning orientation of Si ($\langle 0\,1\,1\rangle_{Si}$) (marked with B in Fig. 1a). Viewed from the $[0\,1\,1]_{Si}$ zone axis, the Si particle appears twinned, as shown in Fig. 1b. However, most Si twinning occurred along only one special plane (i.e. $\{1\,1\,1\}_{Si}$), rather than significantly multiply twinned. The formation of the single twinned Si particle can be attributed to higher quenching rates during melt spinning. It also suggests that Si twinning may be a natural process during nucleation and growth of Si, independent of the modifying elements, because the Al–5Si–5 ppm P alloy does not contain any modifying elements (i.e. Na, Sr), even at a very low level. This suggestion is consistent with the previous report on a so-called "quenching modification" [12] and can be attributed to the TPRE growth mechanism at high undercoolings [3,4]. The high resolution STEM high angle annular dark-field (HAADF) image taken from the boundary (marked with D in Fig. 1b) indicates that the Si particle maintains a perfect cube-to-cube relationship with the α-Al matrix, i.e. $\{1\,1\,1\}_{Si}\langle 0\,1\,1\rangle_{Si}//\{1\,1\,1\}_{\alpha\text{-Al}}\ \langle 0\,1\,1\rangle_{\alpha\text{-Al}}$. This observation is also fully consistent with our previous selected area diffraction pattern (SADP) analyses in Al–5Si alloy [39]. Fig. 1c shows an intersection of Si twins, as marked with C in Fig. 1b. It should be noted that when Si twins of $\{1\,1\,1\}_{Si}$ planes are viewed along the $\langle 0\,1\,1\rangle_{Si}$ directions, the intersection of the $\{1\,1\,1\}_{Si}$ planes corresponds to the TPRE location. The marked intersection of Si twins in the two-dimensional TEM image in Fig. 1b is just the projection along the TPRE [15]. When the electron beam is parallel to the $\langle 0\,1\,1\rangle_{Si}$ directions, it can stimulate

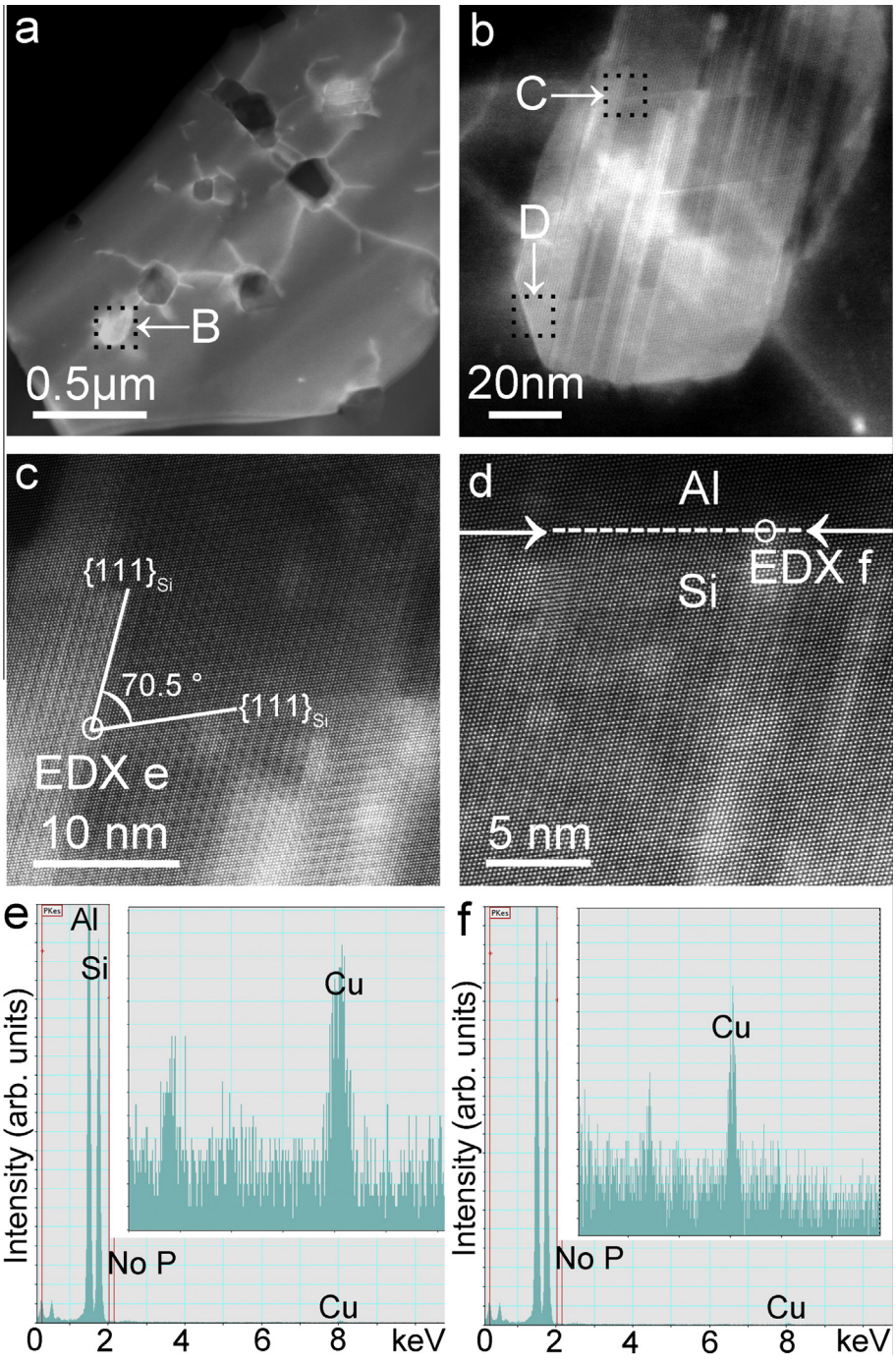

Fig. 1. (a) A low-magnification STEM-HAADF image of Si particles, tilted to the $\langle 0\,1\,1\rangle_{Si}$ zone axis, in Al–5Si–5 ppm P alloy, (b) enlarged area of region (B) (marked with a black box in (a)) showing twins in a single direction, (c) enlarged area of region (C) (marked with a black box in (b)) showing the intersection of Si twins, (d) enlarged area of region (D) (marked with a black box in (b)) showing the interface between Si and α-Al matrix, (e f) EDX analyses taken from the areas as marked in (c, d), respectively.

the EDX signals from atoms adsorbed along the TPRE. The small beam size (0.1 nm) permits the measurement along the column of atoms and facilitates a high response of one atom within the activated volume. It should be also noted that, due to the close Z (atom number) of Al (13) and Si (14), no significant contrast in STEM mode was observed. However, careful observations show that there is a contrast difference at the interface between the Si and Al, as marked with a dashed white line and two white arrows in Fig. 1d. Al appears to be darker than Si. The EDX analyses taken from the intersection of Si twins (Fig. 1e), as marked in Fig. 1c, and the interface between Si particle and Al matrix (Fig. 1f), as marked in Fig. 1d, show only Cu. This Cu signal was detected as an artefact which can be attributed to the available Cu impurity in high-purity Al (5 N) and/or the Cu ring supporting the

TEM sample. No significant Fe or any other element was detected, indicating that the sample is of high purity. It should be noted that Al and Si peaks are always present (Fig. 1e and f); however, for clarity, only the EDX peaks for Fe (~6.398 keV), Cu (~8.04 keV) and Sr (~14.14 keV) are highlighted for the further EDX analyses. It should also be noted that no great difference (i.e. grain size, size and morphology of Si particles) was observed when comparing Al–5Si alloys with and without 5 ppm P addition (not shown here). This indicates that the P addition has no great effect on the growth of eutectic Si during melt spinning. However, DSC analysis indicates that an increasing P level reduces the undercooling of entrained eutectic droplets at slow solidification conditions, as shown in Fig. 2 and Table 1. This indicates that the P addition greatly affects the nucleation of eutectic Si.

3.1.2. DSC analysis

Fig. 2a shows the DSC thermogram for the high purity Al–5Si alloy without any addition, but with a low concentration of 0.4 ppm P only (5 N Al + 5 N Si) resulting from the intrinsic remaining P content of the high purity Al (5 N). The first sharp exotherm A occurred with an onset temperature of 575.5 °C, which is 1.5 °C less than the equilibrium eutectic temperature as documented by Murray and McAlister [40], whilst the small exotherm B occurred with an onset temperature of 544.5 °C. Undercooling is defined here as the difference between the onset temperatures of the grain boundary eutectic peak and droplet peak. This leads to somewhat smaller undercoolings as reported by Ho and Cantor [17], who used the equilibrium eutectic temperature of 577 °C. Exotherm A represents the solidification of grain boundary eutectic, which was already confirmed by Ho and Cantor [17,27] using entrained droplet experiments combined with microstructural characterization. The undercooling (Δ T) was measured to be ~31.0 °C (5 N Al + 5 N Si) and ~20.5 °C (5 N Al + 4 N Si), respectively. The entrained droplet undercooling decreases significantly from 31.0 °C to 20.5 °C when a lower grade Si (4 N) is used. This decrease in undercooling has been associated by Ho and Cantor [17] as an effect of P contamination of the Si used.

Table 1 lists the measured undercoolings from DSC solidification exotherms for the P addition in high purity Al–5Si alloy. An addition of 0.5 ppm P results in the exotherm B occurring with an onset temperature of 559.9 °C. Undercooling was ~16.1 °C. With 3 ppm P addition, the formation of a shoulder in the eutectic droplet peak (exotherm B) was observed to be just after the solidification of the grain boundary eutectic exotherm A (Fig. 2b). Deconvolution of the peak gives a rough estimated onset temperature of the entrained droplet peak of ~575 °C, which is approximately identical to the grain boundary eutectic onset temperature [37]. With 5 ppm P addition, the entrained eutectic droplet peak vanished. Only one exothermic peak (A) is evident, which corresponds mainly to the solidification of grain boundary eutectic overlapping the smaller entrained eutectic peak.

3.1.3. Microstructure after heating

Fig. 3a shows the droplet size distributions of high-purity Al–5Si alloy after controlled heating (from 400 °C to 600 °C), holding (1 min at 600 °C) and cooling (from 600 °C to 400 °C) in the DSC at a rate of 10 °C min^{-1}. Randomly distributed entrained eutectic droplets are evident in the Al matrix and located at the grain boundary, as shown in Fig. 3b. The size of these eutectic droplets is ~21.65 ± 9 μm, as measured from at least 100 eutectic droplets, although their number decreases by Ostwald ripening. A decoration of Si particles can also be observed along the interface between the Al matrix and the entrained eutectic droplet, as shown in Fig. 3c. Small Si particles are located between the Al matrix and the entrained eutectic droplet, while large eutectic Si particles are distributed within the entrained eutectic droplet. The detailed nucleation analysis is discussed in Section 4.2.

3.2. Sr additions

3.2.1. As-spun ribbon microstructure

The addition of Sr into high purity Al–5Si alloys promotes Si twinning during solidification. In contrast to Fig. 1 (without Sr addition), most Si particles were multiply twinned. Fig. 4 shows a series of STEM–HAADF images of a multiply twinned Si particle in high purity melt-spun Al–5Si–200 ppm Sr alloy, viewed in $\langle 0\,1\,1\rangle_{Si}$ directions. In order to highlight Si twins within the Si crystal, a corresponding dark-field image is also shown in Fig. 4b. The faceted morphology of the twinned Si particle can be understood in terms of the interfacial energies between Si and Al [39]. There are two distinct areas, as marked with C and D in Fig. 4a and b, respectively. At the area C, the angle between the two different $\{1\,1\,1\}_{Si}$ planes is close to 70.5°. The intersection of Si twins was highlighted in Fig. 4c. As expected, Sr-rich clusters (Al–Si–Sr) were observed at the intersection of $\{1\,1\,1\}_{Si}$ twins, viewed in the $\langle 0\,1\,1\rangle_{Si}$ directions. A Sr peak (1.88 ± 0.02 wt.%) was observed only at the intersection of Si twins, as shown in the EDX spectra (Fig. 4e). In a region free of crystallographic defects (i.e. free of Si twins), no similar Sr peak can be observed. As described above, Al and Si peaks are not shown in the range of 6–14 keV. Only the peaks of Cu and Sr are highlighted. Because this sample has been mounted on a Cu ring, the Cu signal in the EDX spectra is an artefact and not related to the local composition. The adsorption of Sr at the intersection of $\{1\,1\,1\}_{Si}$ twins is indicative of the IIT mechanism.

At the area D, EDX analysis (Fig. 4f) taken from the area marked with a circle in Fig. 4d shows a stronger Sr peak (3.17 ± 0.26 wt.%). Similar EDX point results can be found along the $\langle 1\,1\,2\rangle_{Si}$ growth direction of Si, as marked with a white arrow in Fig. 4d. The Si twins grow through propagation by the TPRE mechanism [10]. Thus, Sr atoms decorate the $\langle 1\,1\,2\rangle_{Si}$ growth direction of Si. This is indicative of the poisoning of the TPRE mechanism, promoting further Si twins. Furthermore, as described above

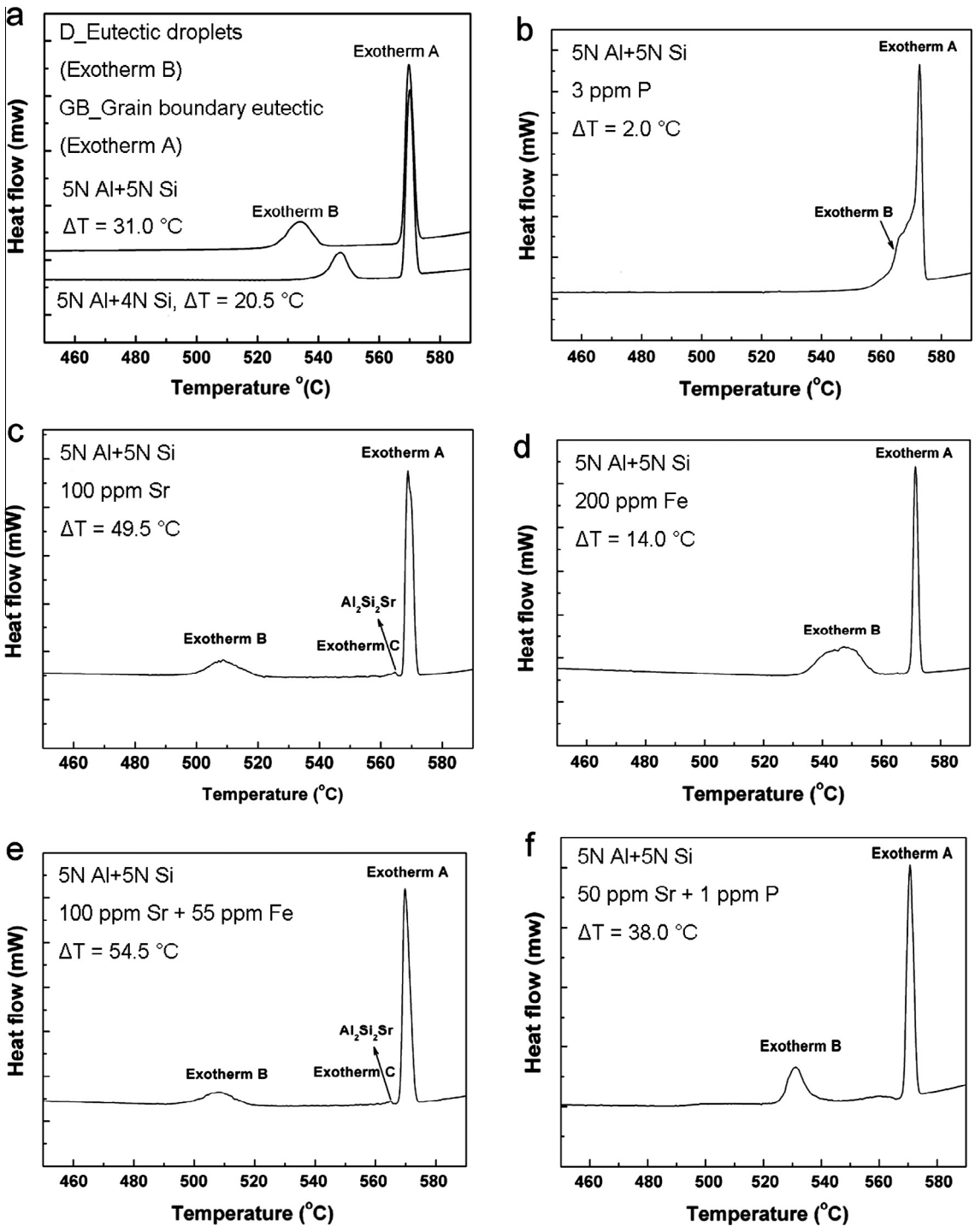

Fig. 2. DSC solidification exotherms of Al–5Si alloys without and with the additions of Sr, Fe and/or P at a cooling rate of 10 °C min^{-1}: (a) 5NAl + 5NSi, 5NAl + 4NSi, (b) 3 ppm P addition, (c) 100 ppm Sr addition, (d) 200 ppm Fe, (e) 100 ppm Sr and 55 ppm Fe addition and (f) 50 ppm Sr and 1 ppm P addition.

(Section 3.1.1), both the intersection of Si twins for IIT and the corner for the TPRE, viewed in the $\langle 0\,1\,1\rangle_{Si}$ directions, appear as single points. Although the crystallographic orientation and location of the TPRE mechanism is identical to that of the IIT mechanism and cannot be excluded by crystallography alone, the IIT segregation pattern is that of a "single" cluster enriched with Al, Si and Sr, while the TPRE segregation pattern is that of clusters along the $\langle 1\,1\,2\rangle_{Si}$ growth direction of Si. Thus, it is important to note that poisoning of the TPRE and IIT mechanisms can be active during Si growth. The marked circles in Fig. 4c and d are only to highlight the investigated areas, but are

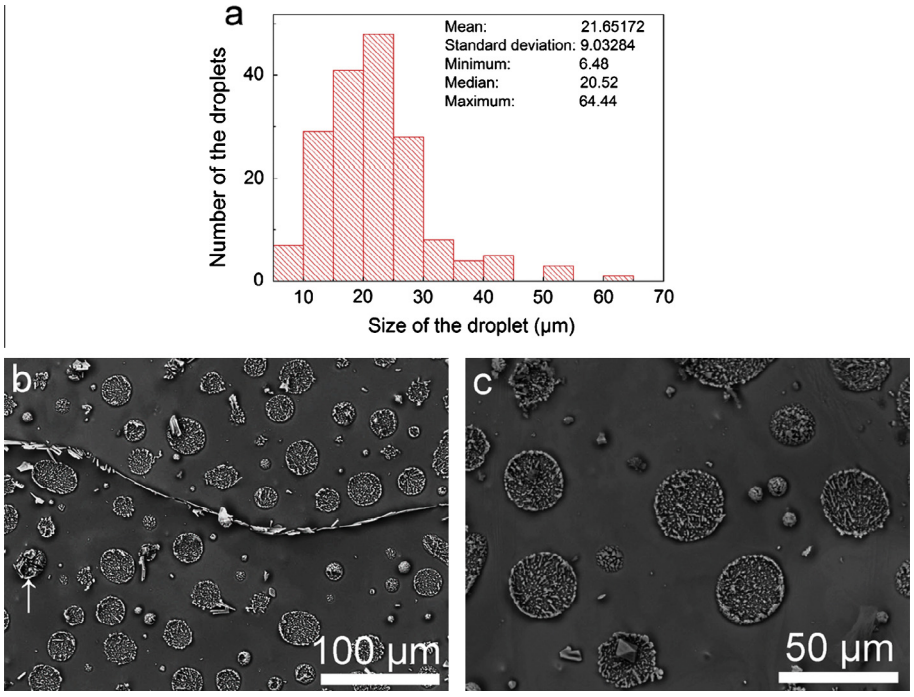

Fig. 3. (a) Size distributions of eutectic droplets within the Al matrix, (b, c) SEM backscattered images showing the eutectic droplets within the Al matrix and along the grain boundary in Al–5Si alloy after heating in DSC.

much larger than the actual beam size. At higher Sr concentrations (i.e. 200 ppm), Al_2Si_2Sr particles were also observed (not shown here) [37] in TEM and DSC analysis.

3.2.2. DSC analysis

Table 1 lists the measured undercooling from DSC solidification exotherms for the Al–5Si alloy containing 20 ppm Sr only. It should be noted that exotherm B occurred with an onset temperature of 526 °C with an undercooling of 49.5 °C. This indicates that the nucleation of the entrained droplets started at a very high undercooling. The same effect was observed with the 50 ppm Sr addition. By increasing the Sr addition to 100 ppm or more, no significant increase in the entrained eutectic droplet undercooling was observed; however, a new peak emerged on the DSC trace with the onset temperature of 566.5 °C (Fig. 2c). This exotherm C may represent the precipitation of the highly undercooled Al_2Si_2Sr phase within the Al–5Si alloys. It should be noted here that the presence of the Al_2Si_2Sr phase is expected above the eutectic reaction in equilibrium conditions. However, because of the high purity elements used here, no significant nucleation sites for the Al_2Si_2Sr phase appear to be present.

3.3. Fe additions

3.3.1. DSC analysis

Table 1 lists the measured undercoolings from DSC solidification exotherms for Al–5Si alloys with Fe additions. In contrast to the Sr addition, no significant decrease in undercooling was observed with the 25 ppm Fe addition. The onset temperature for exotherm B remains unchanged when compared with Al–5Si alloy without any addition. A slight decrease in the undercooling was observed by increasing the Fe addition from 25 ppm to 55 ppm. A further increase in Fe content to 75 ppm does not lead to a significant decrease in the undercooling. A noticeable small decrease in the undercooling was observed with the 200 ppm Fe addition (Fig. 2d). The exotherm B occurred with an onset temperatures of 566.5 °C. The overall undercooling was found to be 14 °C. 2000 ppm Fe addition (Table 1, No. 14), which can be present in commercial purity alloys, results in no further decrease in the undercooling of exotherm B. Instead, new exotherms were observed (not shown here). This infers that at higher Fe levels some other Fe intermetallics precipitate, but they do not contribute significantly to the nucleation of Si, which is fully consistent with our microstructure observation [39]. Overall, the observed undercooling for the entrained eutectic droplet with Fe addition remains largely unaffected, compared to Sr and/or P addition, suggesting little or no influence of low Fe additions on the nucleation of Si. The β-Al_5FeSi phase appears to have no significant effects on the nucleation of eutectic Si [39], compared to P addition, as shown in the DSC analysis (Fig. 2b and d).

3.4. A combined additions of Sr and Fe

3.4.1. As-spun ribbon microstructure

Fig. 5a shows a heavily multiply twinned Si particle ~400 nm in size obtained from melt-spun Al–5Si–100 ppm Sr–55 ppm Fe alloy. Fig. 5b shows the SADP taken by tilting to the $\langle 0\,1\,1\rangle_{Si}$ zone axis with double

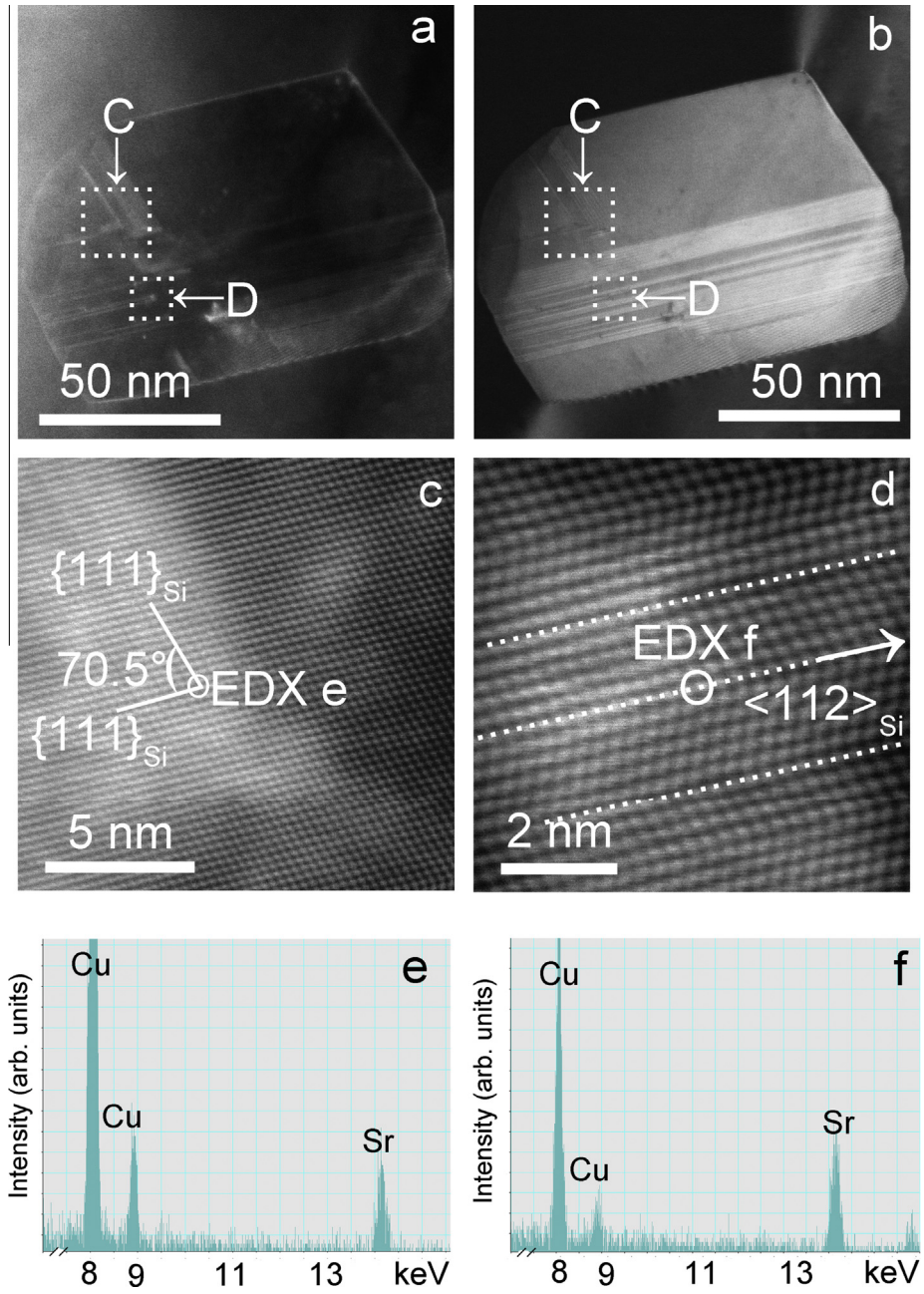

Fig. 4. (a) A low-magnification STEM–HAADF image of a multiple twinned Si particle, tilted to the $\langle 0\,1\,1\rangle_{Si}$ zone axis, in Al–5Si–200 ppm Sr alloy, (b) a corresponding dark-field image, (c) enlarged area of region (C) (marked with a white box in (a)) showing a Sr-rich cluster at the intersection of Si twins, (d) enlarged area of region (D) (marked with a white box in (a)) showing a Sr-rich cluster along the $\langle 1\,1\,2\rangle_{Si}$ growth directions of Si, (e, f) EDX analyses taken from the areas as marked in (c, d), respectively.

diffractions of two variants. Fig. 5c and d shows the central dark field images taken from two different diffraction spots corresponding to two different variants, as marked in Fig. 5b. Both Si variants grow along the $\langle 1\,1\,2\rangle_{Si}$ directions, which is the representative growth direction of the TPRE mechanism. If poisoning of the TPRE occurs, Sr atoms or Sr-rich clusters would be expected to be incorporated along the $\langle 1\,1\,2\rangle_{Si}$ growth directions of Si. While the IIT mechanism occurs, Sr atoms or Sr-rich clusters would be expected at the intersection of two Si variants forming an angle of ~70.5°, as marked in Fig. 5a. In order to elucidate the location and distribution of Sr within the Si crystal, Fig. 6 shows a series of STEM–HAADF images of a multiply twinned Si particle at a low (Fig. 6b and d) and higher (Fig. 6e and f) magnification. Two corresponding dark-field images at a low (Fig. 6a) and high (Fig. 6c) magnification are also shown in order to present the location of the TPRE and the intersection of Si twins. For clarity, the location of the TPRE and the intersection of Si twins are also marked in Fig. 6c. Very interestingly, much more Sr-rich clusters were observed with Fe addition, as compared with Al–5Si–200 ppm Sr alloy without Fe addition (Fig. 4),

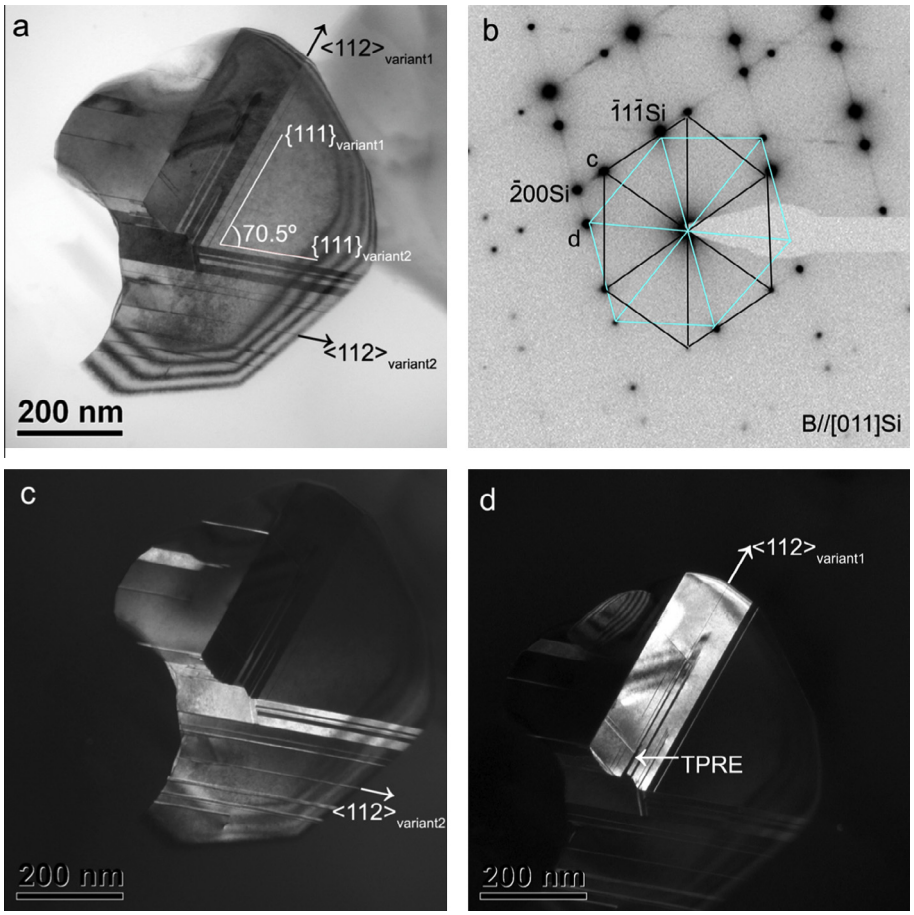

Fig. 5. (a) TEM bright field image of a multiple twinned Si particle, tilted to the $\langle 0\,1\,1\rangle_{Si}$ zone axis, in Al–5Si–100 ppm Sr–55 ppm Fe alloy, (b) corresponding selected area diffraction pattern showing two variants, (c, d) central dark field images taken from the two $\{1\,1\,1\}_{si}$ spots of the two variants, as marked in (b).

indicating that the Fe addition may enhance the influence of Sr. Similar to Fig. 4, two large Sr-rich clusters (Al–Si–Sr–Fe) were also observed in Fig. 6c and d. The first Sr-rich cluster (marked with a white box and an arrow as E in Fig. 6c, and highlighted in Fig. 6e) is located at the intersection of two $\{1\,1\,1\}_{Si}$ twins forming an angle of ~109.5°, suggesting that IIT changes the growth direction. Subsequently, a typical TPRE growth in the new $\langle 1\,1\,2\rangle_{Si}$ growth direction can be observed, as shown in Fig. 6e and f. The second Sr-rich cluster, as marked with a black arrow in Fig. 6c, is also located at the intersection of two $\{1\,1\,1\}_{Si}$ twins. A stronger Sr peak (4.13 ± 0.32 wt.%) was observed in these Sr-rich clusters, as shown in EDX spectra (Fig. 6g). Furthermore, smaller Sr-rich clusters (Al–Si–Sr–Fe) were also observed (Fig. 6f) along the $\langle 1\,1\,2\rangle_{Si}$ growth direction of Si, as marked with a white box and an arrow as F in Fig. 6c, and highlighted in Fig. 6f. A weaker Sr peak (0.08 ± 0.05 wt.%), compared with Fig. 6g, was observed in the corresponding EDX spectra, as shown in Fig. 6h. Similar to Fig. 4, this demonstrates again that both IIT and poisoning of the TPRE mechanisms can be active during the Si growth. All other unmarked peaks except for Fe are coming from W, which may be due to the W tip of the arc melter.

The detected Fe (5.71 ± 0.30 wt.%) peak in Fig. 6g is due to the trace addition of Fe (55 ppm) and the segregation of Fe at the intersection of $\{1\,1\,1\}_{Si}$ planes. The Fe level is a local composition measured by the very limited spot size (0.1 nm) used here as described above. It has been reported that Si has a limited or no solubility of Fe [41]. Here, the higher Fe levels (i.e. 55 ppm) force the segregation ahead of the solid interface, which is entrained by the growing $\{1\,1\,1\}_{Si}$ plane. Furthermore, TEM shows no indication of any Fe-containing intermetallic, but only local Fe-rich clusters within Si.

3.4.2. DSC analysis with an addition of Sr and Fe

Compared to a single addition of Sr (i.e. 200 ppm Sr), a further increase in the undercooling was observed in the case of combined additions of Fe and Sr, as listed in Table 1 (Nos. 15, 16). This suggests that Fe addition, in the presence of Sr, leads to the largest undercooling in entrained eutectic droplets. Exotherm B occurred with an onset temperature of 520.9 °C; undercooling was ~54.6 °C with the addition of 55 ppm Fe and 20 ppm Sr. The undercooling remained unchanged with a constant Fe addition and increasing Sr additions from 20 ppm to 100 ppm. On the basis of these results, it can be concluded that the

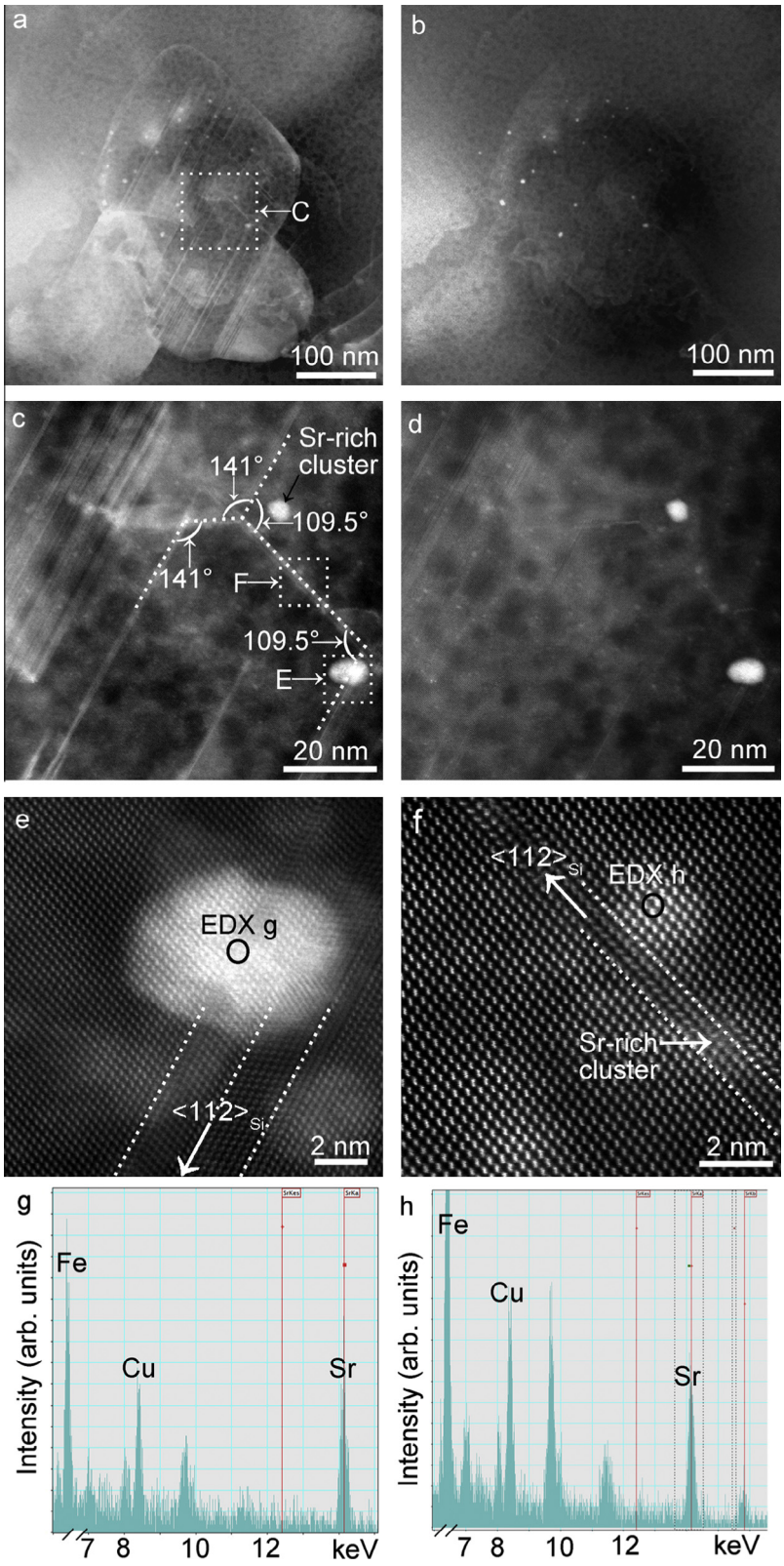

Fig. 6. A series of images taken from a multiply twinned Si particle, tilted to the $\langle 0\,1\,1\rangle_{Si}$ zone axis, in Al–5Si–100 ppm Sr–55 ppm Fe alloy: (a) a dark-field image at a low magnification, (b) a corresponding STEM–HAADF image at a low magnification, (c) an enlarged dark-field image showing multiple Si twins, taken from the area (C) (marked with a white box in (a)), (d) a corresponding STEM–HAADF image, (e) an enlarged STEM–HAADF image taken from the area (E) (marked with a white box in (c)) showing a Sr-rich cluster at the intersection of Si twins, (f) an enlarged STEM–HAADF image taken from the area (F) (marked with a white box in (c)) showing a Sr-rich cluster along the $\langle 1\,1\,2\rangle_{Si}$ growth directions of Si, (g, h) EDX analyses taken from the areas as marked in (e, f), respectively. A Sr-rich cluster at the intersection of Si twins is also marked with a black arrow in (c).

undercooling increases with a combined addition of Fe and Sr. The increase of undercooling can be directly related to our observation in Fig. 6, in that much more Sr-rich clusters (compared with Fig. 4, 200 ppm Sr addition) were observed. Clearly, there is an important interaction between Sr and Fe, which needs to be taken into consideration. The influence of the increased number density of Sr-rich clusters on Si growth is a subject of further investigation.

3.5. Combined addition of Sr and P: DSC analysis

In contrast to the single addition of Sr (i.e. 200 ppm), a combined addition of Sr and P does not produce a significant difference in microstructure, both in the melt-spun condition and after heating in the DSC. Thus, no image of the microstructure is shown here. A combined addition of P and Sr, when excess Sr is present, leads to a high undercooling, as listed in Table 1 (No. 17). A combined addition of P (1 ppm) and Sr (50 ppm) results in the occurrence of exotherm B with an onset temperature of 539.0 °C (much lower than 575 °C, with 1 ppm P addition) (Fig. 2f). Undercooling is ~38.0 °C, but not as high as 49.5 °C with 20 ppm Sr addition (Table 1, No. 6). This can be directly attributed to the interactions between P and Sr, as discussed in Section 4.1.

4. Discussion

4.1. Nucleation sites for Si

In eutectic droplets, Si crystals are distributed along the interfaces between eutectic droplets and the Al matrix (Fig. 3). It is well established that AlP is a potent nucleation site for eutectic Si [17,19,20]. Ho and Cantor [17] proposed that Al combined with P forms an adsorbed AlP layer which subsequently nucleates Si at the Al–eutectic droplet interfaces. A random distribution of Si particles inside the droplets suggests that multiple nucleation of Si is possible. A high nucleation site density at the interface between the droplet and the Al matrix may also explain the multiple nucleation of Si [26], as shown in Fig. 3b and c. The curvature of the droplet is significantly bigger than that of the nucleating Si. Therefore, no significant curvature effect can be implied.

P content is a main controlling factor determining the eutectic droplet undercooling. A lower P content promotes the nucleation of Si at a higher undercooling. The increase in the eutectic droplet undercooling with the addition of only 20 ppm Sr (Table 1) suggests that Sr exerts a negative influence on the potency of AlP compounds. This may be due to the fact that Sr combines with P to form Sr_3P_2 compounds in competition with AlP, or the competition to Al_2Si_2Sr intermetallic with Si to form on AlP, as suggested by Cho et al. [18]. The assumption that Al_2Si_2Sr interacts with AlP appears to be invalid at lower Sr contents, i.e. 20 and 50 ppm, since no peak of Al_2Si_2Sr was observed. Thus, the Al_2Si_2Sr compound cannot stimulate the nucleation of eutectic Si in the droplet. Moreover, at higher Sr levels, the Al_2Si_2Sr intermetallic precipitates before the solidification of exotherm B, but the undercooling remains unchanged (Table 1). If the Al_2Si_2Sr intermetallic interacts or nucleates on AlP patches on the Al interface, the undercooling of the entrained Al–Si eutectic should further increase; however, this is not the case. Furthermore, thermodynamic calculations [37] predict the Al_2Si_2Sr phase to form well above the equilibrium liquidus of the Al–Si eutectic (577 °C). However, this was not observed in the present high purity Al–5Si alloys, suggesting that no sufficient nucleant is present to nucleate the Al_2Si_2Sr phase. This could be different from commercial purity alloys. In addition, even when the Al_2Si_2Sr phase is present at higher Sr levels, it does not appear to contribute to the nucleation of eutectic Si within the entrained droplets. Turnbull and Vonnegut [22] proposed an equation to calculate the disregistry (δ) between substrate and nucleating phases:

$$\delta = \frac{|a_s - a_c|}{a_c} \times 100\% \quad (1)$$

where a_s and a_c are the interatomic/interplanar distances of substrate and crystallization planes, respectively. Due to the high disregistry on close packed planes between the Si and Al_2Si_2Sr intermetallic (22.8%, Table 2), it is highly unlikely that the Al_2Si_2Sr intermetallic acts as nuclei for Si. Zhang and Cantor [26] observed Al_4Sr at higher additions of Sr (3000 ppm), which was supposed to stimulate the nucleation of Si during solidification. However, no evidence of the Al_4Sr phase was observed in this work. This also negates the hypothesis proposed by Zhang and Cantor [26]. A high disregistry (17.7%, Table 2) between Al_4Sr and Si phase further weakens this argument.

Overall, it is suggested that, at low Sr concentrations, the undercooling increases mainly because of the lack of AlP due to the formation of Sr_3P_2 compound. Although there is a lack of strong experimental support for the existence of the Sr_3P_2 phase in Al–5Si based alloys considering the expected level of P (less than 5 ppm), the possible existence of the Sr_3P_2 phase can be strongly supported in terms of the thermodynamics of competing phosphide compounds, i.e. the formation of Na_3P [17] in the case of Na addition.

Fig. 7 shows a Gibbs free enthalpy (ΔG) of formation vs. temperature (T) plot in the form of an Ellingham diagram for different phosphide compounds of potential modifying elements normalized to 1 mol of P. Thermodynamic data for the enthalpy of formation and entropy of formation were reviewed and assessed by Schlesinger [42]. It is noteworthy that a considerable scatter has been documented in the reported data, in particular for Na_3P and Sr_3P_2. Within the Ellingham diagram, it is apparent that all phosphide compounds exhibit a near identical slope entropy of formation of ~10 kJ mol^{-1} K^{-1}. This value was assumed for the unknown entropy of formation of Na_3P and Sr_3P_2 phases, as shown with dotted lines in Fig. 7. The

Table 2
Crystallographic data and calculated disregistry to Si for selected phases on closely matched planes.

No.	Phase	Crystal structure	Lattice parameter (nm)	Disregistry, δ (%)
1	Al	Cubic	$a = 0.40491$	25.3
2	Si	Cubic	$a = 0.5421$	–
3	Al_2Si_2Sr	Hexagonal	$a = 0.41872$, $c = 0.7427$	22.8
4	Al_4Sr	Body-centered tetragonal	$a = 0.4460$, $c = 1.1070$	17.7
5	AlP	Cubic	$a = 0.5431$	0.18
6	Sr_3P_2	Cubic	$a = 0.932$	71.9

Note: $(0001)[1120]_{Al2Si2Sr}//(111)[011]_{Si}$, $(111)[011]_{Al,AlP,Sr3P2}//(111)[011]_{Si}$, and $(001)[011]_{Al4Sr}//(111)[011]_{Si}$ is applied to calculate the lattice disregistry with Si (diamond cubic).

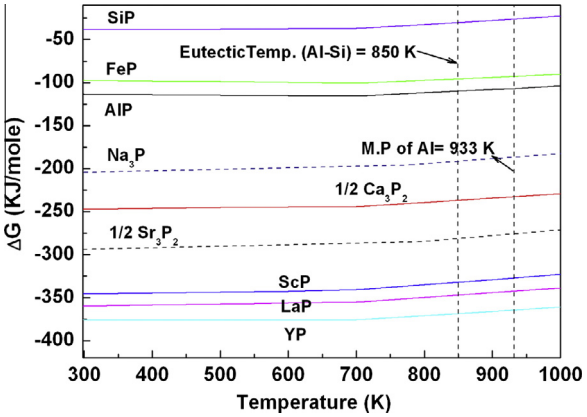

Fig. 7. Gibbs free enthalpy of phosphide compounds, ΔG^0, vs. temperature for 1 mol of P. Note: The graph was drawn using the ΔG^0 equations and values as documented by Schlesinger [42].

Ellingham diagram clearly shows that Sr_3P_2 and Na_3P compounds have a lower ΔG than AlP, indicating that the Sr_3P_2 and Na_3P compounds are thermodynamically more stable and must be preferentially formed. It is well established [17,27] that Na addition poisons the AlP with the formation of Na_3P. Ho and Cantor [17] measured undercooling (~8 °C) with the 80 ppm Na addition in an Al–Si alloy containing only 0.5 ppm P, which is approximately the same P level present in the alloys under our investigation. However, 49.5 °C undercooling was observed with only 20 ppm Sr addition. It can be thus inferred that Sr_3P_2 is the dominant reactant as compared to Na_3P. This supports the hypothesis that the formation of the Sr_3P_2 compound will consume P and forces the nucleation of Si to higher undercoolings. It should be also noted that some other phosphides, i.e. YbP, YP, LaP and ScP, have an even more negative ΔG and have been reported to cause higher undercoolings, and thus refinement of eutectic Si [43,44].

It is worth pointing out that just because a compound is more stable, the less stable phase is not fully transformed. The equilibrium reaction ($AlP \leftrightarrow Al + P$) determined the AlP available for Si nucleation. However, because of the interaction between AlP and Sr_3P_2 phase ($2AlP + 3Sr \leftrightarrow Sr_3P_2 + 2Al$), the effective concentration of P varies greatly with respect to the original concentration. This effective concentration can be measured by the activity coefficient. The equilibrium fractions between the competing phases establishes itself by the well-known formula [45,46]:

$$k_{AlP} = a_{AlP}/x_{AlP} = \frac{\text{Effective concentration of AlP}}{\text{Real concentration of AlP}} \quad (2)$$

where a_i and k_{AlP} are activity and kinetic coefficient, respectively. This formula determines the remaining AlP, which can form patches to nucleate Si in the droplet. However, activities (a_i) and kinetic coefficients (k_{AlP}) are often not known for phosphide compounds. Thus, despite the presence of more stable phosphide compounds, AlP patches will still be present. Their amount could be estimated if the thermodynamic data are known. Their size or size distribution will be dependent on adsorption kinetics such as a line tension and other effects [17].

Other phosphide compounds competing with AlP such as oxyphosphates, i.e. Na_3PO_4, Sr_3PO_4 and YPO_4, have not been considered here. They are expected only to form at the melt surface and would not be expected to contribute to the nucleation of Si within the bulk material. No other oxide compounds were observed experimentally here. The likelihood of obtaining oxide bi-films is remote during melt spinning because the thin ribbon geometry (80 μm thickness) and the reduced He pressure will guarantee laminar flow despite high wheel speeds. Thus, the nucleation kinetics can be interpreted purely by the competing phosphide compounds.

4.2. Nucleation kinetics

4.2.1. Classical nucleation theory

To understand the observed undercooling of Al–Si entrained droplets, nucleation kinetics need to be elucidated.

The nucleation kinetics of entrained droplets have been described by Kim et al. [47]. It was postulated that at the peak of the entrained droplet exotherm the steady state nucleation rate I is related to the fraction of untransformed droplets Z as:

$$dZ/dt = I(1 - Z) \quad (3)$$

where dZ/dt is the solidification rate, Z is the solid fraction of eutectic liquid droplets, and I is the nucleation rate within each particle.

Using $\Delta s_f = L_m/T_{eq}$ (Δs_f is the entropy of fusion), I can be given as:

$$I = \frac{N_c k_B T}{h_P} \exp\left(-\frac{16\pi\gamma^3 T_{eq}^2 f(\theta)}{3k_B L_m^2 (T_{eq}-T)^2 T}\right) \exp\left(-\frac{\Delta g_v}{k_B T}\right) \quad (4)$$

where k_B is the Boltzmann constant (1.38×10^{-23} J K^{-1}), h_P is the Planck constant (6.63×10^{-34} J s), N_c is the number of potential nuclei at the solid–liquid interface per droplet, T is the temperature, T_{eq} is the equilibrium melting temperature (577 °C), L_m is the latent heat of fusion (4.61×10^9 J m^{-3}) [21], γ is the solid–liquid interfacial energy (0.352 J m^{-2}) [21], θ is the contact angle at the solid–nucleus–liquid triple point and Δg_v is the driving force for nucleation of Si in the eutectic liquid droplets by the surrounding Al matrix. $\exp\left(-\frac{\Delta g_v}{k_B T}\right)$ is ~0.01 for most of the metals [17,48].

Eq. (4) is valid under the assumptions that: (i) all the droplets have the same size ($d_{droplet}$) and hence the same equilibrium melting temperature, T_{eq}, (ii) all the droplets solidify instantaneously after nucleation, and (iii) droplets are spherical in shape.

At a given cooling rate $R = -dT/dt$, the particle solidification rate has its maximum value when

$$d/dT(dZ/dt) = -R^{-1} dZ^2/dt^2 = 0 \quad (5)$$

In the DSC traces, it is related to the peak temperature of the exotherm B.

Differentiating Eq. (4) with respect to T will give

$$dI/dt = I^2 \quad (6)$$

Inserting $dI/dt = -R dI/dT$ in Eq. (6) gives

$$-R\, dI/dT = I^2 \quad (7)$$

where R is the imposed cooling rate in the DSC.Using classic nucleation theory [22], with $T = T_p$, and the expressions for A and B, Eq. (7) simplifies to Eq. (8):

$$\ln\left(\frac{A}{B}\right) + \ln\left(\frac{R(3T_P - T_{eq})}{T_P^2 (T_{eq}-T_P)^3}\right) = \left(\frac{-A}{(T_{eq}-T_P)^2 T_P}\right) \quad (8)$$

where $A = \left(\frac{16\pi\gamma^3 T_{eq}^2 f(\theta)}{3 k_B L_m^2}\right)$, $B = \frac{N_c k_B T}{h_P} \exp\left(-\frac{Q}{k_B T}\right)$.

Eq. (8) should give a straight line with a negative slope of $-A$ and an extrapolated y-intercept of $\ln(B/A)$ taking $\ln\left(\frac{R(3T_P - T_{eq})}{T_P^2 (T_{eq}-T_P)^3}\right)$ on the abscissa and $\left(\frac{1}{T_P (T_{eq}-T_P)^2}\right)$ as the ordinate. The negative slope of $-A$ is sensitive to the contact angle, which permits the contact angle (θ) to be calculated after rearranging the expression for A and applying Eq. (9) for a spherical cup:

$$f(\theta) = \frac{(2+\cos\theta)(1-\cos\theta)^2}{4} \quad (9)$$

The y-intercept permits the calculation of nucleation site densities (N_c) after rearranging the expression for B.

According to Kim et al. [47], the data were plotted, as shown in Fig. 8, for high purity Al–5Si alloy (5 N Al + 5 N Si, lower P, i.e. 0.4 ppm P), medium purity Al–5Si alloy (5 N Al + 4 N Si, higher P, i.e. 5 ppm P), high purity Al–5Si–20 ppm Sr alloy and high purity Al–5Si–20 ppm Sr–55 ppm Fe alloy, respectively. The slope of the curve has the opposite sign to that expected for the classical nucleation theory. However, the slope permits the interpretation of a wetting angle of ~16° for high purity Al–5Si alloy, indicating that the acting substrate for Si is still highly effective. The intersection with the y-axis gives the number of sites involved in the Si nucleation. However, the resulting numbers of –12.44 (high purity Al–5Si alloy), –13.29 (medium purity Al–5Si alloy), –14.4 (high purity Al–5Si–20 ppm Sr alloy) and –11.58 (high purity Al–5Si–20 ppm Sr–55 ppm Fe alloy), are far smaller than 1 nucleation site. As Ho and Cantor have argued in a previous publication [17], this can be regarded as an indication that the physical description of the classical nucleation theory based on a continuum approach does not hold for a small contact angle below 30°. Clearly, a better model is required to elucidate the nucleation kinetic of Si. Although adsorption has been modeled by Kim and Cantor [49] for hypothetical binary alloy systems, this has not been done for real alloy systems. Recent progress in the description of rate-limiting processes during grain refinement of Al has identified the free growth criterion as a key to understanding the critical onset of growth [35,36,48]. Thus, the free growth concept is used here to elucidate the nucleation kinetics of entrained eutectic Si in Al–Si based alloys.

4.2.2. Free growth model

Analogous to the mercury experiments carried out by Turnbull [50], heterogeneous patches can be highly efficient sites for nucleation. Similar to the nucleation and free growth of Al on active TiB_2 particles, the size of AlP patches or AlP particles and their size distribution are proposed to become rate limiting steps [35,36,48] (see Appendix A). Free growth away from the AlP patches or AlP particles occurs when the critical size of Si nucleation sites is identical to the equivalent size of the AlP patches or AlP particles, given by:

$$\Delta T = \frac{4\gamma}{\Delta S d_{patch}} \quad (10)$$

where γ is the solid–liquid interfacial energy for Si (3.52×10^{-1} J m^{-2}) [21], ΔS is the entropy of fusion per unit volume for Si (0.7279×10^7 J K^{-1} m^{-3}) [21] and d_{patch} is the AlP patch or AlP particle size. This indicates that a critical undercooling is related to the AlP patch size or AlP particle size at higher P concentrations.

In the previous research [17,47], a defined size of the nucleation site was often proposed. For a given undercooling, once the size of the nucleation size (d_{max}) fulfils the free growth criterion, the nucleus can continue to grow. However, it should be noted that if a size distribution of the sites is supposed, for each range of the size distribution, heterogeneous nucleation occurs essentially instantaneously at a given undercooling (ΔT^{Heter}), and

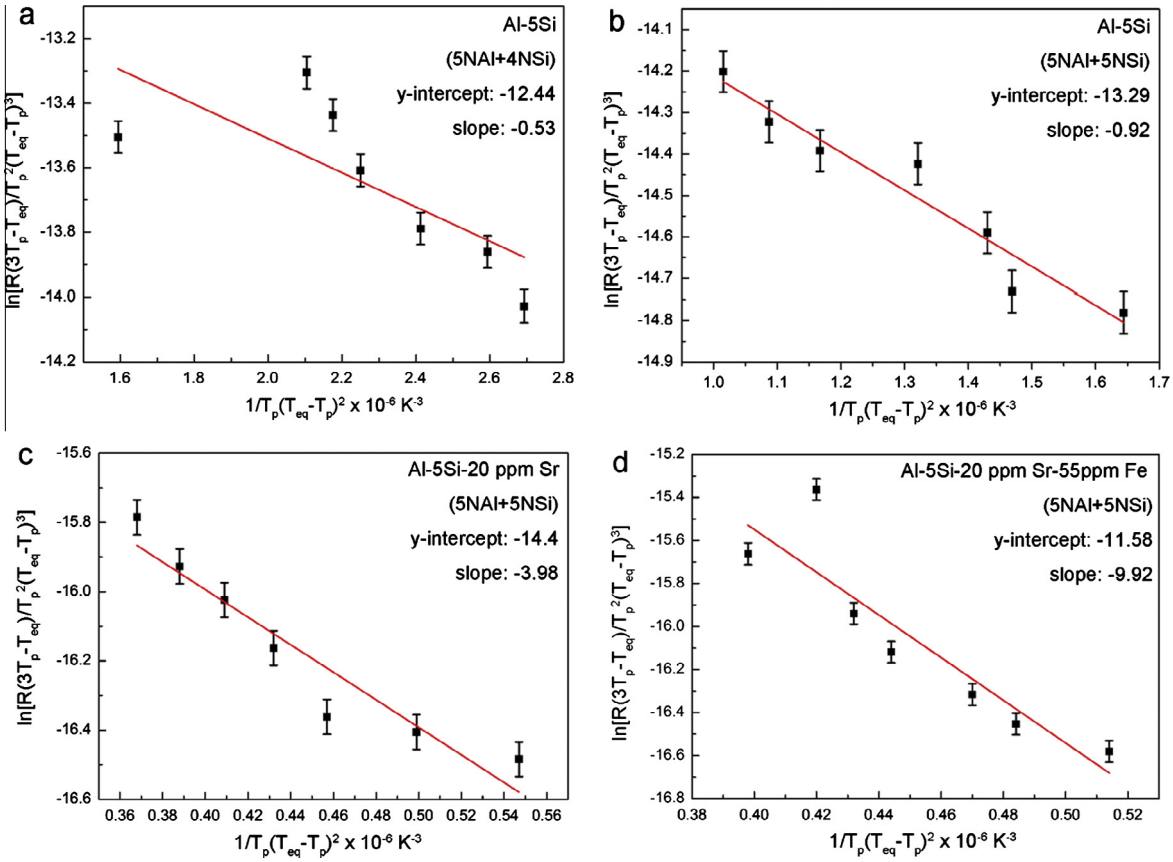

Fig. 8. Classical nucleation plots extracted from (a) high purity Al–5Si alloy (5 N Al + 5 N Si, lower P, i.e. 0.4 ppm P), (b) medium purity Al–5Si alloy (5 N Al + 4 N Si, higher P, i.e. 5 ppm P), (c) high purity Al–5Si–20 ppm Sr alloy and (d) high purity Al–5Si–20 ppm Sr–55 ppm Fe alloy, respectively.

independently of the substrate size [51]. The nuclei formed on these sites in such a range of size distributions can only grow when a critical undercooling (ΔT_{growth}) is achieved. Thus, using Eq. (10), the discrete distribution of the particles can also be directly related to a discrete distribution of growth undercooling.

Furthermore, the heat flow or heat release during nucleation and free growth can be reflected in DSC traces. The measured DSC solidification exotherm (Fig. 2) shows a much broader peak and is nearly symmetric, further indicating that a size distribution of the particles and thereby a distribution of undercooling should be taken into consideration. By analysis of the exotherm shape in DSC, it is possible to experimentally measure the relevant parameters for nucleation.

A Gaussian distribution of heterogeneous nucleation sites inside the melt [51] was employed for modeling purposes:

$$\frac{dn}{d(\Delta T)} = \frac{n_{\max}}{\Delta T_\sigma \sqrt{2\pi}} \exp\left[-\frac{1}{2}\left(\frac{\Delta T - \Delta T_0}{\Delta T_\sigma}\right)^2\right] = \frac{1}{R}\frac{dn}{dt} = \frac{I}{R} \tag{11}$$

where $n_{\max}$ is the total density of the available sites within one droplet, whilst ΔT_0 is the mean value of distribution and $\Delta T_\sigma$is the standard deviation [51]. These parameters must be measured experimentally. For the imposed cooling in DSC, I is the nominal nucleation rate and R is the imposed cooling rate.

In DSC traces, ΔT_0 is taken as the difference between the equilibrium melting temperature (T_{eq}, 577 °C) and the peak temperature of the exotherm B (T_P), while ΔT is taken as the difference between the equilibrium melting temperature (T_{eq}, 577 °C) and the temperatures ranging from the onset temperature (T_{onset}) and the peak temperature (T_P) of the exotherm B. Assuming a Gaussian distribution of undercooling (Eqs. (10) and (11)), ΔT_σ is taken as one-third of the difference between the onset temperature (T_{onset}) and the peak temperature (T_P) of the exotherm B. According to this definition, ~99.7% of the area of the exotherm B is covered. The remaining area (less than 0.15%) is of the same order of magnitude as the resolution of the DSC itself.

Fig. 9 shows the onset temperature (T_{onset}), the peak temperature (T_P) and the end temperature (T_{end}) of the exotherm B for high purity Al–5Si alloy (5 N Al + 5 N Si, lower P, i.e. 0.4 ppm P), medium purity Al–5Si alloy (5 N Al + 4 N Si, higher P, i.e. 5 ppm P), high purity Al–5Si–20 ppm Sr alloy and high purity Al–5Si–20 ppm Sr–55 ppm Fe alloy, respectively. For each alloy, the onset temperature (T_{onset}) exhibited only a slightly negative change with increasing cooling rate, while the peak temperature (T_P) shifted to a lower temperature with increasing cooling rate. The shift of exotherm B (T_P) can be attributed

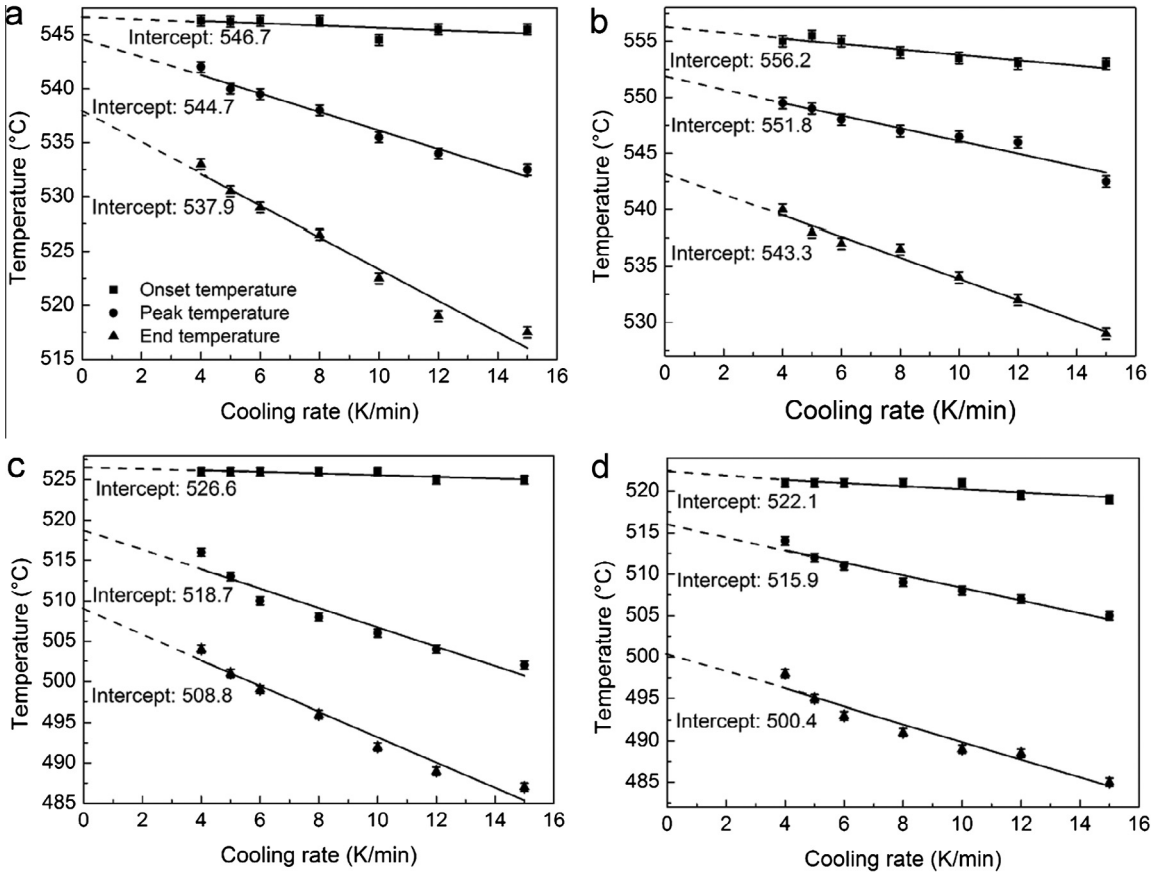

Fig. 9. Variations of the onset temperature, the peak temperature and the end temperature of the exotherm B in DSC curves with the cooling rates: (a) high purity Al–5Si alloy (5NAl + 5NSi, lower P, i.e. 0.4 ppm P), (b) medium purity Al–5Si alloy (5NAl + 4NSi, higher P, i.e. 5 ppm P), (c) high purity Al–5Si–20 ppm Sr alloy and (d) high purity Al–5Si–20 ppm Sr–55 ppm Fe alloy.

to the heat release coming from the entrained droplets in which Si nucleation may be delayed as (i) not all P is formed into an AlP patch for a given droplet and (ii) the shift depends on the nucleation and growth of the AlP patch. In order to obtain the equilibrium peak temperature, the intercept of peak temperature is used at a cooling rate approaching zero, as marked with a dashed line in Fig. 9. It also indicates that the peak temperature (T_P) of the exotherm B in DSC curves cannot be directly related to the maximum undercooling for Si nucleation. It is proposed that the maximum free growth undercooling is obtained before the peak temperature (T_P) of the exotherm B, at which the maximum transformation occurs.

It is important to note that the free growth model does not have a steady nucleation rate. At a given temperature interval, a number of AlP patches or AlP particles will fulfil the free growth criterion from which free growth of Si can occur. Thus, the free growth criterion has to be considered. Applying the approach by Kim et al. [47] for droplet nucleation kinetics and using the free growth criterion according to Eq. (10), yields

$$\frac{dI}{d\Delta T} = \frac{Rn_{\max}}{\Delta T_\sigma \sqrt{2\pi}} \exp\left[-\frac{1}{2}\left(\frac{\Delta T - \Delta T_0}{\Delta T_\sigma}\right)^2\right]\left[-\left(\frac{\Delta T - \Delta T_0}{\Delta T_\sigma^2}\right)\right] \tag{12}$$

Inserting Eqs. (11) and (12) into Eq. (7) gives

$$\ln\left(-\frac{\Delta T - \Delta T_0}{\Delta T_\sigma}\right) + \frac{1}{2}\left(\frac{\Delta T - \Delta T_0}{\Delta T_\sigma}\right)^2 = \ln\left(\frac{n_{\max}}{\sqrt{2\pi}}\right) \tag{13}$$

From Eq. (13), it is very clear that the maximum nucleation sites ($n_{\max}$) within one droplet are directly related to the size distribution of AlP particles or AlP patches for Si nucleation (ΔT_0 and ΔT_σ), but independently of the cooling rates. On the other hand, the size distribution of AlP particles or AlP patches depends on the available P content in a given droplet. As an initial assumption, only one AlP patch for each droplet is formed (see Appendix A). Thus, this indicates that the maximum number of nucleation sites ($n_{\max}$) is dependent on the size distribution of droplets and P content. This is fully consistent with the free growth model, but is in contrast to Eq. (8), where cooling rates (R) are included. According to the definition of the undercooling distribution as described above in DSC traces, the calculated maximum nucleation site value ($n_{\max}$) is $\sim 6.77 \times 10^2$.

For a given droplet size, a higher P concentration (e.g. 5 ppm, medium purity Al–5Si alloy) results in a larger AlP patch (see Appendix A). More nucleation sites can be activated at a lower undercooling. In contrast, the decreasing number of nucleation sites for a higher

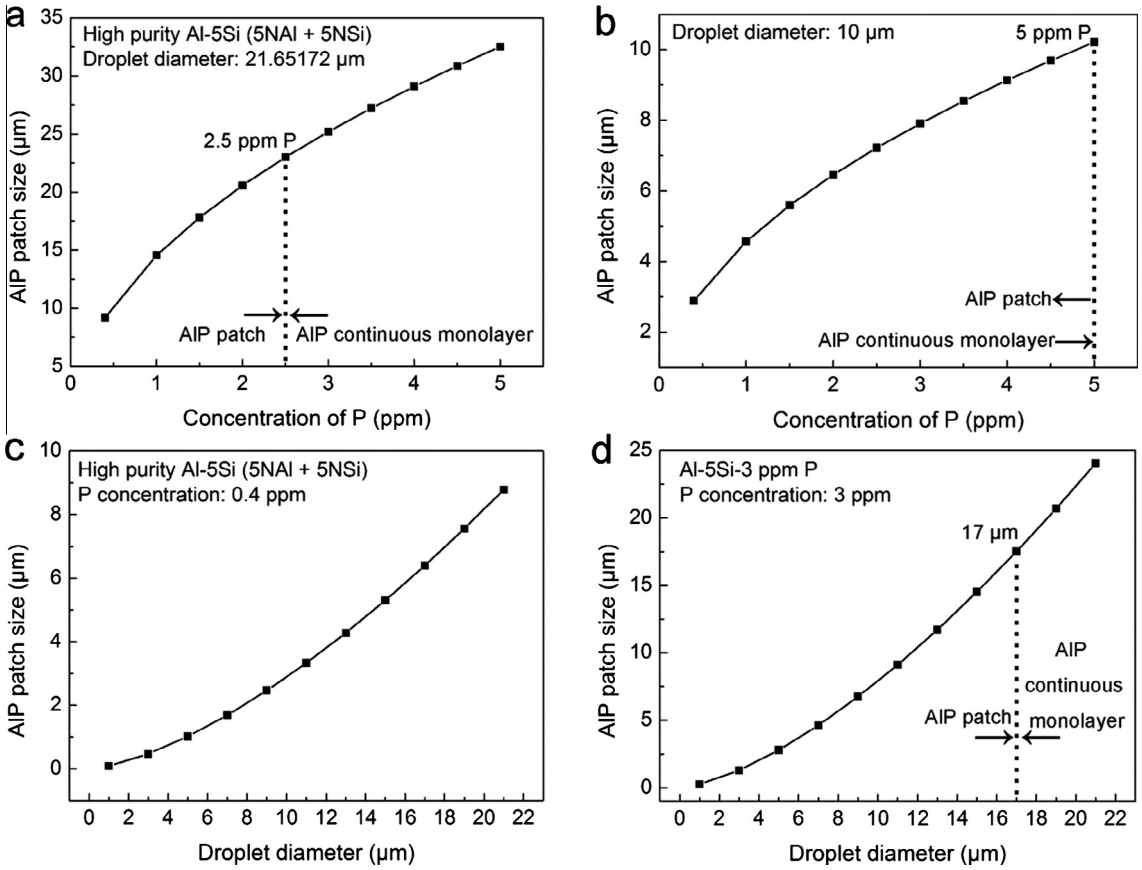

Fig. 10. (a, b) Variations of AlP patch sizes with P contents for given droplet diameters (~21.6 μm and 10 μm), respectively. (c, d) Variations of AlP patch sizes with droplet sizes for given P concentrations (0.4 ppm and 3 ppm), respectively.

undercooling can be directly related to the limiting AlP patch size for Si nucleation. Thus, the limiting step for the growth of Si on AlP patches can be regarded as the free growth criterion.

4.2.3. Determination of AlP patch size

In the case of a single patch in a droplet, the patch distribution is determined by the distribution of eutectic droplet if P is uniformly distributed within all eutectic droplets. The volume of eutectic can be calculated using the level rule and phase diagram [40] (see Appendix A). For the near zero solubility of P in solid Al, and if all P is segregated into the eutectic, an enrichment of P occurs in droplets by a factor of 3.

An estimation of the AlP patch size (Eq. (14)) is possible under the assumption that (i) only one AlP patch is present in a given entrained eutectic droplet, (ii) no P is in solution within the Al matrix, and (iii) all P is within the entrapped liquid in the entrained droplets and in grain boundary eutectic [17].

$$d_{patch} = 0.144429\sqrt{d_{droplet}^3 P_{concentration}} \quad (14)$$

In Eq. (14), three parameters are included. For a given droplet diameter ($d_{droplet}$, μm), which can be measured experimentally (e.g. ~21.6 μm for high purity Al–5Si alloys in Fig. 3), the AlP patch size (d_{patch}, μm) can be calculated as a function of $P_{concentration}$, as shown in Fig. 10a. It is clear that AlP patch size increases with increasing P concentration. This is fully consistent with the fact that more P atoms are present in a larger droplet, thus forming a larger AlP patch. When the P concentration is over 2.5 ppm, the predicted AlP patch area (1661 μm^2) is significantly large enough to completely cover the droplets (1472 μm^2, 21.6 μm), thus forming a AlP continuous monolayer around the interface between droplets and the matrix. With decreasing droplet size (e.g. $d_{droplet}$ = 10 μm), a smaller AlP patch size is predicted, as shown in Fig. 10b. Furthermore, a higher P concentration (e.g. 5 ppm) is required to form an AlP continuous monolayer around the interface between droplets and the matrix. For clarity, Fig. 11 shows schematically the nucleation events inside the droplet for different P concentrations. At higher P concentrations, separate AlP particles may form within a given droplet, as shown in Fig. 11a. Nucleation and growth of Si will readily occur on these AlP particles because of their large size and high nucleation potency. At low P concentrations, AlP cannot form as separate AlP particles, but will form as an AlP layer on Al. The AlP layer may be continuous at significantly high P concentrations, as shown in Fig. 11b, but may also break up into individual AlP patches at even lower P concentrations, as shown in Fig. 11c. Nucleation of Si

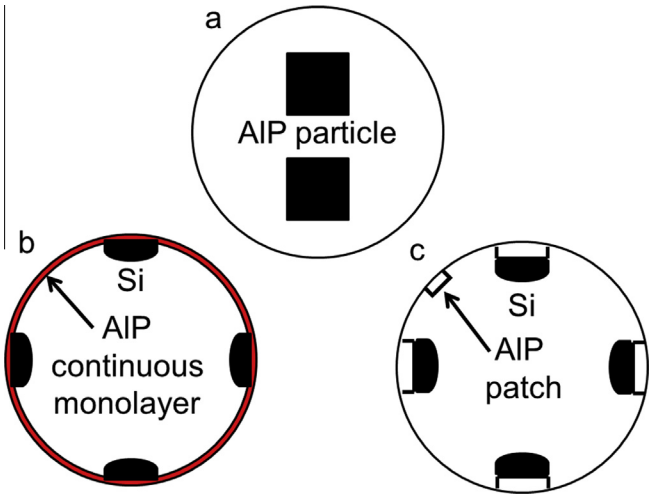

Fig. 11. (a) Schematic diagrams of nucleation events inside the droplet for different P concentrations: (a) at higher P concentrations, separate AlP particles may form; (b, c) at low P concentrations, AlP cannot form as separate AlP particles, but will form as a AlP layer on Al. The AlP layer may be continuous at significant high P concentrations (b), but may also break into individual AlP patches at even lower P concentrations (c).

will occur readily on all AlP, which may be present as AlP monolayers and AlP patches, respectively. However, free growth of Si can only occur on the largest AlP layers or AlP patches, depending on the required undercooling (ΔT). Furthermore, it should be noted that the droplet size distribution is dependent only on the initial rapid solidification condition and subsequent Ostwald ripening during heating and holding being kept constant. However, the droplet size is also a factor affecting the formation of the AlP monolayer or AlP patch. At a lower P content, if the droplet size is large enough, the formation of an AlP continuous monolayer is also possible. However, the number of AlP continuous monolayers decreases with decreasing P content.

For a given $P_{concentration}$ (ppm), which can also be measured experimentally (e.g. 0.4 ppm in high purity Al–5Si alloy, Table 1), the AlP patch size (d_{patch}, μm) can be calculated with the function of the droplet size ($d_{droplet}$), as shown in Fig. 10c. At a lower P concentration (0.4 ppm), the AlP patch cannot cover the interface completely between droplets and the matrix, forming an AlP patch with defined droplet size. However, at a higher P concentration (3 ppm), the formation of a complete AlP continuous monolayer is possible when a droplet size is larger than 17 μm, as shown in Fig. 10d. Thus, because of the volume-to-surface ratio, a larger droplet volume can more easily segregate a complete AlP monolayer on the surface of the droplet.

According to Eqs. (14) and (10), the AlP patch size can also be directly related to the observed undercooling (ΔT). Taking high purity Al–5Si alloy (with 0.4 ppm P) as an example, the mean droplet size is ~21.6 μm (experimentally measured from high purity Al–5Si alloy with 0.4 ppm P, Fig. 3b). The predicted AlP patch size is ~8.79 μm. Inserting $d_{patch} = 8.79$ μm into Eq. (14), a very small undercooling (0.02 K) is obtained for Si nucleation.

The measured undercooling (ΔT) in high purity Al–5Si alloy (0.4 ppm P) is ~31 °C. Furthermore, the measured undercooling (ΔT) in Al–5Si–20 ppm Sr alloy is ~49.5 °C because of the reduction of AlP caused by the formation of Sr_3P_2. For both cases, the required AlP patch size for Si nucleation is ~5.69 nm and 3.564 nm, respectively. This is much smaller than the predicted values in Fig. 10, indicating that the AlP patch size is sufficient for the free growth of Si to occur on the AlP substrate inside the droplet for more than one Si particle.

The great difference between measured undercooling (31 °C) and predicted undercooling (0.02 °C) in high purity Al–5Si alloy strongly indicates that some difficulties exist during the AlP formation and subsequent Si nucleation. Firstly, not all the P atoms segregate together to form a single AlP patch, which is in contrast to our initial assumption. The formation of many smaller separate AlP patches may also be possible. Secondly, not all the AlP patches can grow Si freely. For a given undercooling, only an AlP patch with a size larger than the critical size, which is determined by Eq. (10), can promote Si nucleation. Thirdly, the formation of an AlP patch is also dependent on the line tension. A higher line tension between the droplet and the matrix increases the tendency to form AlP patches, thus increasing the AlP patch size.

5. Conclusions

(1) While conditions to facilitate the observation of nucleation were optimized in entrained droplet experiments, the observed mechanisms are also valid at moderate cooling conditions, such as in shape casting.
(2) In high purity melt-spun Al–5Si alloys without Sr addition, the TPRE mechanism results in a quenching modification and a lower density of Si twins, when compared with Sr additions, leading to a higher density of multiple Si twins.
(3) With the addition of Sr, both IIT growth mechanism and poisoning of the TPRE growth mechanism were observed, suggesting that both mechanisms are active during Si growth.
(4) A combined addition of Sr and Fe results in the formation of heavily multiply-twinned Si as well as an increased undercooling, indicating that Fe addition may enhance the influence of Sr on the modification of eutectic Si.
(5) Sr addition exerts no positive effect on the nucleation process, while an increased undercooling was observed. This can be attributed to the formation of Sr_3P_2 having a lower ΔG and is preferentially formed as compared to other competing phosphide compounds, i.e. AlP.

(6) Only a trace P addition has a profound effect on the Si nucleation. The estimated AlP patch size was found to be sufficient for the free growth of Si to occur within the droplets, which strongly indicates that the nucleation of Si on AlP patch or AlP particle is a limiting step for free growth.

Acknowledgments

J.H.L. acknowledges Prof. Gerhard Dehm for granting access to TEM at the Erich Schmidt Institute of Materials Science of the Austrian Academy of Science. M.Z. Zarif acknowledges financial support from the Higher Education Commission (HEC) of Pakistan and cooperation from the OEAD.

Appendix A. Determination of AlP patch size

In order to estimate the AlP patch size in a given droplet, an even segregation of P is assumed in entrained eutectic droplets and at grain boundary eutectic. The lever rule at eutectic temperature (577 °C) gives 33.3 wt.% eutectic containing all the P. For a given P concentration (e.g. 1 ppm, 1×10^{-6}), this indicates that three times the P concentration (e.g. 3 ppm, 3×10^{-6}) is segregated in entrained eutectic droplets and at the grain boundary eutectic.

Assuming that droplets are spherical, for a given droplet diameter ($d_{droplet}$, μm), the volume of the droplet can be calculated:

$$Volume = \frac{4}{3}\pi\left(\frac{d_{droplet}}{2}\right)^3 \tag{A.1}$$

Assuming all P is segregated into one spherical droplet with a given diameter ($d_{droplet}$, μm), the volume of the droplet gives the volume of P within the droplet (e.g. 3×10^{-6} Volume). The atomic weight (31) and density (1.82 g cm^{-3}) of P allows us to calculate the number of P atoms within the droplet [21]:

$$P_{atoms} = \frac{\frac{4}{3}\pi\left(\frac{d_{droplet}}{2}\right)^3 \times 10^{-18} \times 3 \times P_{concentration} \times 10^{-6} \times 1.82 \times 10^6}{31} \times 6.0221429 \times 10^{23} \tag{A.2}$$

For AlP with a diamond cubic crystal structure, one P atom combines with one Al atom on {100} plane or other plane (e.g. {111}). Thus, an area of AlP monolayer or AlP patch can be calculated.

$$Area_{AlP} = (a)^2 = (0.5431)^2 = 0.295\,nm^2 \tag{A.3}$$

where a is the lattice parameter in nm.

Multiplying $Area_{AlP}$ with P_{atoms}, total AlP area within the droplet can be calculated. As described above, all P atoms are segregated into one spherical droplet with a given diameter ($d_{droplet}$, μm); further assuming that only one patch forms within the droplet, the AlP patch size (d_{patch}, μm) can be estimated:

$$d_{patch} = 2\sqrt{\frac{Area_{AlP} \times P_{atom}}{\pi}} = 0.144429\sqrt{d^3_{droplet} P_{concentration}} \tag{A.4}$$

Appendix B. Determination of undercooling (ΔT) from the AlP patch size

Undercooling (ΔT) can be directly related to the predicted AlP patch size using Eq. (B.1).

$$\Delta T = \frac{4\gamma}{\Delta S d_{patch}} \tag{B.1}$$

where ΔT is the undercooling (°C), γ is ~0.3524 J m^{-2} [21], ΔS is the entropy of fusion (87.79896 J mol^{-1} K^{-1}) [21] and d is the patch size (m).

In order to transform the unit from J mol^{-1} K^{-1} to J m^{-3} K^{-1}, assuming per unit volume ($1 \times m^3$), it gives:

$$\frac{\rho V}{28} = \frac{2.57 \times 10^6 g/m^3 \times 1m^3}{28} = 0.91 \times 10^5 mol \tag{B.2}$$

Then,

$$1\frac{J}{mol.K} = 0.91 \times 10^5 \frac{J}{m^3.K} \tag{B.3}$$

$$\Delta S_V = 0.91 \times 10^5 \times 87.79896 = 7.9897 \times 10^6 \frac{J}{m^3.K} \tag{B.4}$$

References

[1] Davis JR et al. ASM handbook: casting, vol. 15. 3rd ed. Metals Park, OH: ASM International; 1998. p. 751–3.
[2] Pacz A. U.S Patent No. 1387900; 1921.
[3] Day MG, Hellawell A. Proc R Soc Lond A 1968;305:473–91.
[4] Shamsuzzoha M, Hogan LM. J Crys Growth 1986;76:429–39.
[5] Shamsuzzoha M, Hogan LM. Phil Mag A 1986;54:459–77.
[6] Liu QY, Li QC, Zhang JR. Scripta Metall 1988;22:789–91.
[7] Ransely CE, Neufeld H. ibid 1950–51; 78: 25.
[8] Plumb RC, Lewis JE. J Inst Met 1957-58;86:393–400.
[9] Wagner RS. Acta Metall 1960;8:57.
[10] Hamilton RD, Seidensticker RG. J Appl Phys 1960;31:1165.
[11] Hellawell A. The growth and structure of eutectics with silicon and germanium. Oxford: Pergamon Press; 1970. p. 72.
[12] Shu-Zu Lu, Hellawell A. Met Trans A 1987;18A:1721–33.
[13] Nogita K, Yasuda H, Yoshida K, Uesugi K, Takeuchi A, Suzuki Y, et al. Scripta Mater 2006;55:787–90.
[14] Nogita K, Yasuda H, Yoshiya M, McDonald SD, Uesugi K, Takeuchi A, et al. J Alloys Compd 2010;489:415–20.
[15] Timpel M, Wanderka N, Schlesiger R, Yamamoto T, Lazarev N, Isheim D, et al. Acta Mater 2012;60:3920–8.
[16] Faraji M, Katgerman L. Micron 2010;41:554–9.
[17] Ho CR, Cantor B. Acta Metall Mater 1995;43:3231–46.
[18] Cho YH, Lee HC, Oh KH, Dahle AK. Metall Mater Trans A 2008;10:2435.
[19] Crosley PB, Mondolfo LF. Modern Castings 1966;49:63.
[20] Nogita K, McDonald SD, Tsujimoto K, Yasuda K, Dahle AK. J. Electron Microscopy 2004;53:361–9.
[21] Brandes EA, Smithells CJ, editors. Metals reference handbook. London: Butterworth; 1983. p. 6–29.

[22] Turnbull D, Vonnegut B. Ind Eng Chem 1952;44:1292.
[23] Flood SC, Hunt JD. Met Sci 1981;15:287–94.
[24] Guillet L. Rev Met 1922;19:303.
[25] Campbell J, editor. Complete casting handbook. Oxford: Elsevier; 2011. p. 279–334.
[26] Zhang DL, Cantor B. Metall Trans A 1993;24:1195–204.
[27] Ho CR, Cantor B. J Mater Sci 1995;20:1912–20.
[28] Shankar S, Riddle YW, Makhlouf MM. Acta Mater 2004;52:4447–60.
[29] Shankar S, Riddle YW, Makhlouf MM. Shape casting. San Francisco, CA: TMS International; 2005. pp. 136.
[30] Khalifa W, Samuel FH, Gruzleski JE. Metall Mater Trans A 2003;34:807.
[31] Yang B, Stefanescu D, Leon-Torres J. Metall Mater Trans A 2001;32:3065.
[32] Wang CC, Smith CS. J Met Trans AIME 1950;188:136–8.
[33] Moore KI, Zhang DL, Cantor B. Acta Metall Mater 1990;38:1327–42.
[34] Cantor B, O'Reilly KAQ. Acta Metall Mater 1995;43:405–17.
[35] Quested TE, Greer AL. Acta Mater 2005;53:4643–53.
[36] Quested TE, Greer AL. Acta Mater 2005;53:2683–92.
[37] Zarif M, McKay B, Schumacher P. Metall Mater Trans A 2011;41:1684.
[38] Watanabe M, Williams DB. J Microsc 2006;221:89–109.
[39] Li JH, Zarif M, Dehm G, Schumacher P. Phil Mag 2012;92(31):3789–805.
[40] Murray JL, McAlister AJ. Bull Alloy Phase Diagr 1984;5:74–84.
[41] Newman RC. Rep Prog Phys 1982;45:1163–210.
[42] Schlesinger ME. Chem Res 2002;102:4267–301.
[43] Li JH, Suetsugu S, Tsunekawa Y, Schumacher P. Metall Mater Trans A 2013;44:669–81.
[44] Li JH, Schumacher P. Int J Cast Metal Res 2012;25:347–57.
[45] Porter DA, Easterling KE, editors. Phase transformation in metals and alloys. London, UK: Chapman and Hall; 1992. pp. 185–230.
[46] Smith EB. Basic chemical thermodynamics. Oxford: Oxford University Press; 1973. p. 93.
[47] Kim WT, Zhang DL, Cantor B. Metall Trans A 1991;22A:2487.
[48] Greer AL. Phil Trans R Soc Lond A 2003;361:479–95.
[49] Kim WT, Cantor B. Acta Metall Mater 1994;42:3115–27.
[50] Turnbull D. J Appl Phys 1950;21:1022–8.
[51] Dantzig JA, Rappaz M. Solidification. Boca Raton, FL: CRC Press; 2009. pp. 345–367.